

Antiferroelectric negative capacitance from a structural phase transition in zirconia

Michael Hoffmann^{1,a,‡,*}, Zheng Wang^{2,‡}, Nujhat Tasneem^{2,‡}, Ahmad Zubair³, Prasanna Venkat Ravindran², Mengkun Tian⁴, Anthony Gaskell², Dina Triyoso⁵, Steven Consiglio⁵, Kanda Tapily⁵, Robert Clark⁵, Jae Hur², Sai Surya Kiran Pentapati², Milan Dopita⁶, Shimeng Yu², Winston Chern^{3,7}, Josh Kacher⁸, Sebastian E. Reyes-Lillo⁹, Dimitri Antoniadis³, Jayakanth Ravichandran¹⁰, Stefan Slesazek¹, Thomas Mikolajick^{1,11} & Asif Islam Khan^{2,8,*}

¹NaMLab gGmbH, 01187 Dresden, Germany.

²School of Electrical and Computer Engineering, Georgia Institute of Technology, Atlanta, GA 30332, USA.

³Department of Electrical Engineering and Computer Science, Massachusetts Institute of Technology, Cambridge, MA 02142 USA.

⁴Institute for Electronics and Nanotechnology, Georgia Institute of Technology, Atlanta, GA 30332, USA.

⁵TEL Technology Center, America, LLC, 255 Fuller Rd., Suite 214, Albany, NY 12203, USA.

⁶Department of Condensed Matter Physics, Faculty of Mathematics and Physics, Charles University, Ke Karlovu 5, 12116, Prague, Czech Republic.

⁷Izentis LLC, PO Box 397002, Cambridge, MA 02139, USA.

⁸School of Materials Science and Engineering, Georgia Institute of Technology, Atlanta, GA 30332, USA.

⁹Departamento de Ciencias Físicas, Universidad Andres Bello, Santiago 837-0136, Chile.

¹⁰Department of Chemical Engineering and Materials Science, University of Southern California, Los Angeles, CA 90089, USA.

¹¹Institute of Semiconductors and Microsystems, TU Dresden, Dresden, Germany.

^aCurrently at: Department of Electrical Engineering and Computer Sciences, University of California, Berkeley, CA 94720, USA.

[‡]These authors contributed equally to this work.

*Corresponding authors: (michael.hoffmann190@gmail.com) and (asif.khan@ece.gatech.edu).

Abstract

Crystalline materials with broken inversion symmetry can exhibit a spontaneous electric polarization, which originates from a microscopic electric dipole moment. Long-range polar or anti-polar order of such permanent dipoles gives rise to ferroelectricity or antiferroelectricity, respectively. However, the recently discovered antiferroelectrics of fluorite structure (HfO₂ and ZrO₂) are different: A non-polar phase transforms into a polar phase by spontaneous inversion symmetry breaking upon the application of an electric field. Here, we show that this structural transition in antiferroelectric ZrO₂ gives rise to a negative capacitance, which is promising for overcoming the fundamental limits of energy efficiency in electronics. Our findings provide insight into the thermodynamically ‘forbidden’ region of the antiferroelectric transition in ZrO₂ and extend the concept of negative capacitance beyond ferroelectricity. This shows that negative capacitance is a more general phenomenon than previously

thought and can be expected in a much broader range of materials exhibiting structural phase transitions.

Main text

Antiferroelectric materials are promising for diverse applications ranging from energy harvesting [1] and solid state cooling devices [2] over electromechanical transducers [3] to energy storage supercapacitors [4] [5]. First predicted in 1951 [6], antiferroelectricity was subsequently discovered in the archetypal perovskite oxide, lead zirconate (PbZrO_3) [7] [8]. Ever since, the range of materials has been expanded to two-dimensional hybrid perovskites [9], interfacially engineered heterostructures and superlattices [10], fluorite structure binary oxides [11] [12], and more have been predicted by first principles calculations [13] [14]. However, compared to their ferroelectric counterparts, antiferroelectrics have remained less explored and understood so far, despite their intriguing properties and rich phase transition phenomena [14] [15] [16]. Therefore, antiferroelectric materials hold a large untapped potential for the discovery of novel emergent phases for example in antiferroelectric oxide heterostructures, which have been investigated in this work.

Antiferroelectricity is characterized by a distinctive, double hysteresis loop in the macroscopic electric polarization P vs. electric field E_a characteristics as shown in Fig. 1a based on a Kittel-model (see supplementary section S1) [6]. From a thermodynamic perspective, such a macroscopic response can be described by a free energy (G)-polarization landscape as shown in Fig. 1b for $E_a = 0$, where the only stable state is the macroscopically non-polar ground state (A) at $P = 0$. However, when an electric field $E_a = E_1$ is applied, see Fig. 1c, an energy barrier emerges between the non-polar state M and the polar state N. This 'forbidden' region of negative free energy curvature ($d^2G/dP^2 < 0$) between points B and C is thermodynamically unstable [6] [15]. According to theory, the permittivity and thus capacitance of a material is proportional to $(d^2G/dP^2)^{-1}$, which means that at the antiferroelectric transition the capacitance of the material would become negative if stabilized in a larger system [17] [18]. Due to the inversion symmetry of the non-polar ground state, the same transition occurs when an opposite electric field $E_a = -E_1$ is applied, see Fig. 1d. Therefore, two separate and symmetric regions of negative capacitance can be predicted at the antiferroelectric non-polar to polar phase transition as shown by the dotted lines in Fig. 1a where $dP/dE_a < 0$.

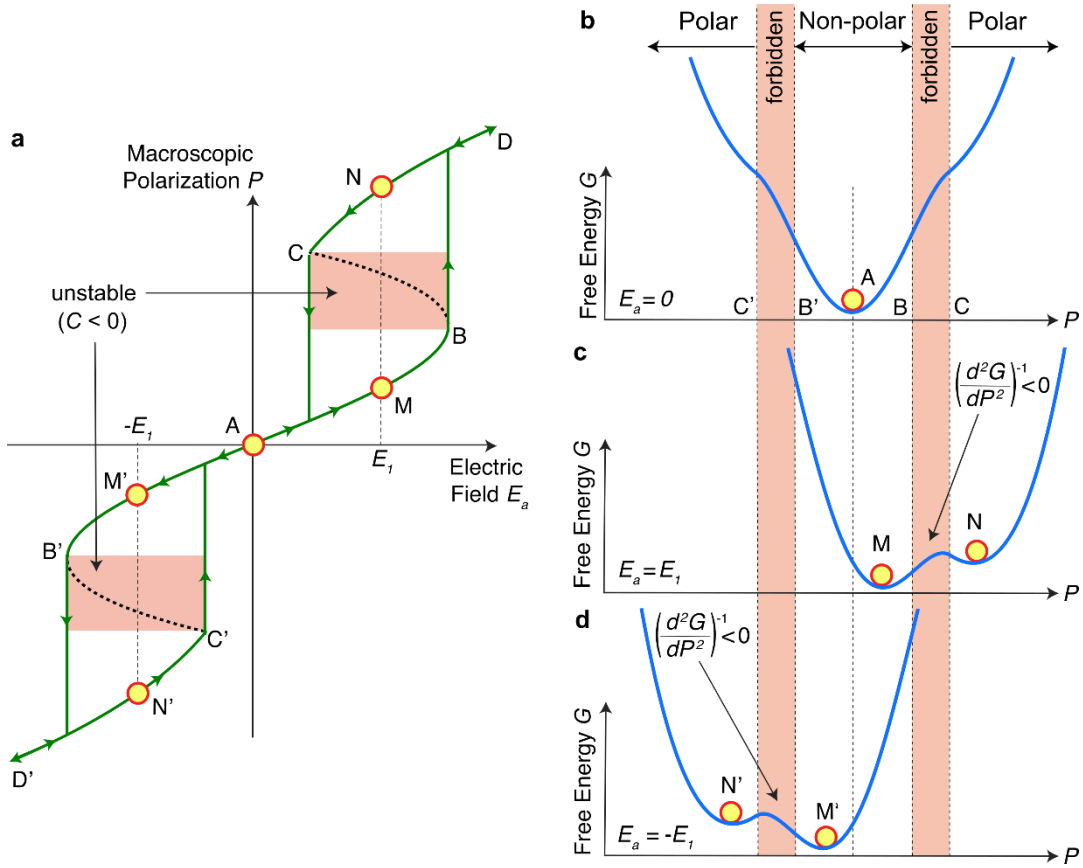


Figure 1. **Origin of antiferroelectric negative capacitance.** **a**, The polarization P -electric field E_a characteristics of an antiferroelectric material. The segment BAB' corresponds to the non-polar, antiferroelectric ground state, and segments CD and $C'D'$ correspond to the polar phase. Segments BC and $B'C'$ represent the unstable negative capacitance regions. At $E_a = E_1$, the antiferroelectric has two stable states: M and N . **b-d**, The antiferroelectric free energy landscape at $E_a = 0$ (b), E_1 (c) and $-E_1$ (d). $d^2G/dP^2 < 0$ in the P -range corresponding to BC and $B'C'$ 'forbidden' regions.

Similar 'S'-shaped P - E curves have been derived from the Landau-Ginzburg-Devonshire theory of ferroelectric phase transitions many decades ago but were previously understood to be inaccessible to experiments due to their unstable nature [19]. Only recently, it was suggested that one could access these 'forbidden' thermodynamic regions in ferroelectric/dielectric heterostructures using pulsed electrical measurements [20] [21]. In such a structure, the positive capacitance of the dielectric layer can stabilize the region of negative capacitance and prevent the screening of bound polarization charge by free electrons in the metal electrodes. Here, we apply a similar approach to first probe the inaccessible region of a non-polar to polar structural phase transition in an antiferroelectric oxide. While experimental insights into such thermodynamic instabilities are of fundamental interest to materials science, they are also useful for prospective applications since the resulting negative capacitance can be used to amplify voltage signals in electronic devices and circuits [18] [22].

Historically, antiferroelectricity has been related to the anti-polar alignment of microscopic electric dipoles in the unit cell [6]. For example, in the ground state of antiferroelectric PbZrO_3 , two adjacent columns of Pb ions point in the same direction, while the next two columns have antiparallel alignment [7]. The application of a sufficiently large electric field then leads to a spontaneous alignment of the anti-parallel dipoles resulting in a transition to a polar ferroelectric state [23]. In contrast, the newly discovered HfO_2 and ZrO_2 based antiferroelectrics of fluorite structure transcend this classical definition of antiferroelectricity [11] [12], since their ground state does not exhibit anti-polar order but is microscopically non-polar [24]. Note that this is fundamentally different from previous investigations in ferroelectrics, where no phase transition or change of symmetry occurs in the 'forbidden' region of the energy landscape [21].

Here, we investigate this unique type of non-polar to polar antiferroelectric transition in ZrO_2 as a model system, which is of significant technological importance due to its compatibility with semiconductor manufacturing and thickness scalability to the nanometer regime [12]. Additionally, no doping of ZrO_2 is needed to induce antiferroelectricity in contrast to HfO_2 based thin films [11] [25]. At room temperature, the stable bulk phase of ZrO_2 is the non-polar monoclinic $\text{P}2_1/\text{c}$ phase, which can be suppressed in thin films of around 10 nm thickness and below, which favor the non-polar tetragonal $\text{P}4_2/\text{nmc}$ phase [12]. An applied electric field of around 2-3 MV/cm can then transform the non-polar tetragonal phase into the polar orthorhombic $\text{Pca}2_1$ phase, which is known to be ferroelectric [26]. While obtaining definitive experimental proof of such a field-induced first-order phase transition has proved difficult so far [27], this mechanism is consistent with first-principles calculations [24] [28] as well as composition- and temperature-dependent experimental results [25]. While the microscopic switching pathway between the $\text{P}4_2/\text{nmc}$ and $\text{Pca}2_1$ phases is still unclear, it has been suggested to include an intermediate phase of orthorhombic $\text{Pmn}2_1$ symmetry for $\text{Hf}_{0.5}\text{Zr}_{0.5}\text{O}_2$ [29].

For basic antiferroelectric characterization, $\text{TiN}/\text{ZrO}_2/\text{TiN}$ capacitors were fabricated as described in methods. Grazing incidence X-ray diffraction (GIXRD) measurement results presented in Supplementary Fig. S1 confirm that the crystalline ZrO_2 layer is in the non-polar tetragonal $\text{P}4_2/\text{nmc}$ phase in the as fabricated capacitors. Fig. 2a and supplementary Fig. S2a show the antiferroelectric double hysteresis loops in the polarization-electric field characteristics for a 10 nm and 5 nm ZrO_2 layer, respectively, measured using a ferroelectric tester. As expected, the ‘forbidden’ regions (see Fig. 1) of the structural transition to the polar orthorhombic $\text{Pca}2_1$ phase cannot be observed electrically due to their instability in a single layer antiferroelectric capacitor. To access these unstable region, a positive series capacitance can be used in the form of a dielectric layer in contact with the antiferroelectric [18] [20] [21].

When the antiferroelectric enters the unstable region in such a heterostructure, the resulting negative capacitance would then increase the total capacitance of the dielectric/antiferroelectric stack beyond than that of the dielectric layer alone. Such a capacitance enhancement would thus be a clear signature of the structural transition itself. To test this prediction, we fabricated heterostructure capacitors consisting of the same ZrO_2 layer and a stack of $\text{Al}_2\text{O}_3/\text{HfO}_2$ dielectrics with TiN used as top and bottom electrodes using atomic layer deposition as described in methods. The intermediate Al_2O_3 layer was introduced to prevent the crystallization of the top HfO_2 layer due to templating effects from the underlying crystallized ZrO_2 . Scanning transmission electron microscopy (STEM) analysis of a representative $\text{TiN}/\text{ZrO}_2/\text{Al}_2\text{O}_3/\text{HfO}_2/\text{TiN}$ heterostructure in Fig. 2b confirms that the ZrO_2 layer was stabilized in its non-polar tetragonal phase while the HfO_2 layer remained amorphous. The combined results of our GIXRD measurements together with STEM and nanobeam electron diffraction data (see Supplementary Fig. S3) present strong evidence for a fully non-polar tetragonal ground state of the ZrO_2 layer.

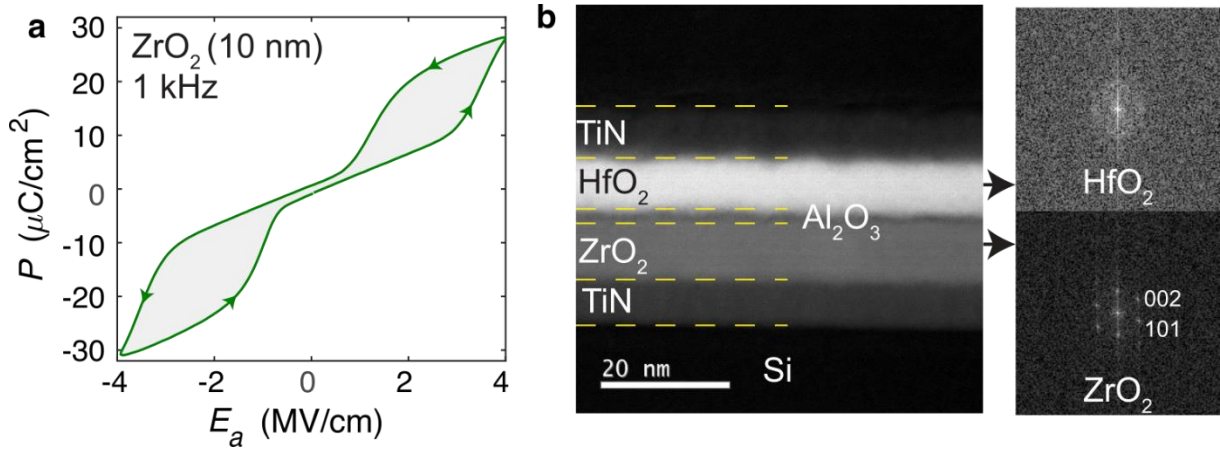


Figure 2. **Standard characterization of antiferroelectric ZrO₂ thin film and heterostructure.** **a**, Polarization P vs. electric field E_a characteristics of a TiN/ZrO₂(10 nm)/TiN capacitor measured using a standard ferroelectric tester at 1 kHz. **b**, Low magnification high angle annular dark field (HAADF) scanning transmission electron microscopy (STEM) image of the cross-section of a representative TiN/HfO₂/Al₂O₃/ZrO₂/TiN heterostructure grown on Si showing all the layers distinguishable with clear interfaces. Fast Fourier transforms of high magnification HAADF-STEM images of the same sample show amorphous rings in the HfO₂ layer and discrete diffraction spots in the ZrO₂ layer consistent with the tetragonal <010> zone axis.

To probe the capacitance of the heterostructure under high applied fields, we adopt a pulsed capacitance measurement technique [20] [30]. We apply microsecond voltage pulses and the charge supplied by the voltage source is directly measured by integrating the measured current. Details are described in methods. Note that standard small-signal capacitance-voltage measurements are too slow at the high applied voltages needed, leading to significant charge injection or dielectric breakdown. In contrast, pulsed capacitance measurements can mitigate this, if the pulse duration is shorter ($\sim 1 \mu\text{s}$ in our experiments) than the time scale for charge injection, breakdown and related mechanisms [20].

Fig. 3a shows the experimental setup in which voltage pulses $V_{in}(t)$ ($t \equiv \text{time}$) of $T = 1.1 \mu\text{s}$ duration, different amplitudes V_a were applied to the capacitors in series to an external resistor R . Waveforms of V_{in} , measured current I , and integrated charge ($=\int I dt$) for different amplitudes V_a for a HfO₂(8 nm)/Al₂O₃(~ 1 nm)/ZrO₂(10 nm) capacitor are shown in Fig. 3b. For a given V_a , Q_{max} is the total charge supplied by the voltage source (i.e., $Q_{max} = \int_0^T I(t) dt$). Q_{res} is the residual charge when V_{in} goes to zero (i.e., $Q_{res} = \int_0^\infty I(t) dt$), and accounts for charge injection and leakage. The difference between Q_{max} and Q_{res} is defined as ΔQ , which is the actual amount of charge that is reversibly delivered to and discharged from the capacitor and determines the differential capacitance of the heterostructure as $C_{DE-AFE} = \Delta Q / \Delta V_a$. Fig. 3c plots Q_{max} , Q_{res} and ΔQ (calculated from Fig. 3b: panel 3) as functions of V_a . We note in Fig. 3c for positive V_a that Q_{res} is zero, and $\Delta Q = Q_{max}$ as expected in the absence of charge injection and leakage for a purely capacitive load. The slope of the ΔQ - V_a curve for $V_a \geq 10$ V (YZ segment) is larger than the capacitance of the constituent dielectric stack C_{DE} which is shown as a slope in Fig. 3c and was measured on a separate HfO₂(8 nm)/Al₂O₃(~ 1 nm) capacitor fabricated under the same processing conditions (see Supplementary Fig. S4). For large negative values of V_a , Q_{res} has a non-zero value; however, accounting for the corresponding charge injection and leakage, a similar capacitance enhancement is observed for $V_a < -9.2$ V (Y'Z' segment).

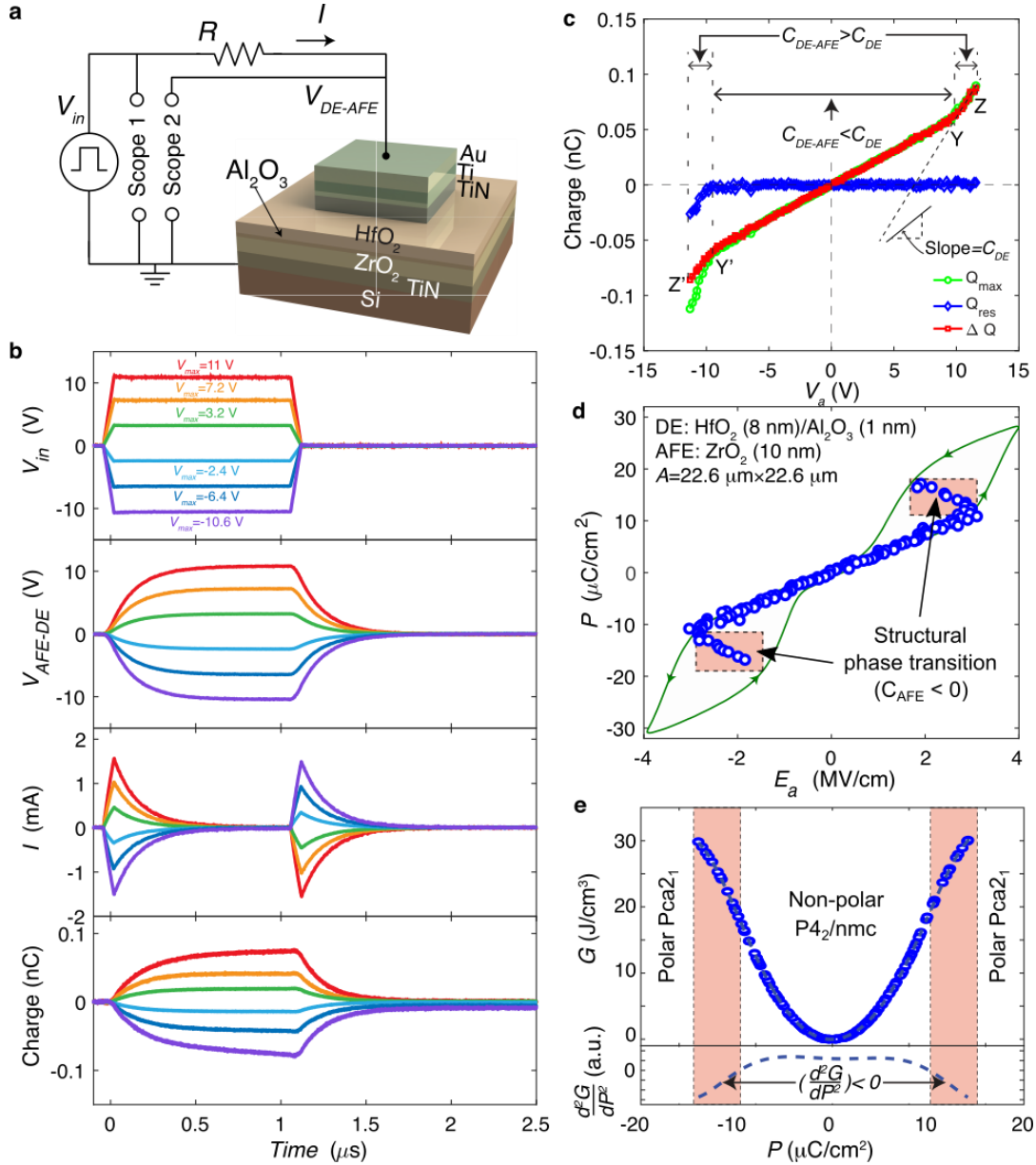


Figure 3. Demonstration of antiferroelectric negative capacitance. **a**, Experimental setup of the pulsed charge measurements on the dielectric-antiferroelectric heterostructure. V_{in} , V_{DE-AFE} , R and I are the applied voltage pulse, the voltage across the DE-AFE capacitor, the series resistor (5.6 k Ω) and the current through R , respectively. The waveforms of V_{in} and V_{DE-AFE} were measured using an oscilloscope at different amplitudes of the V_{in} pulse. **b**, Transient waveforms of V_{in} , V_{DE-AFE} , I and integrated charge for a $\text{HfO}_2(8 \text{ nm})/\text{Al}_2\text{O}_3(\sim 1 \text{ nm})/\text{ZrO}_2(10 \text{ nm})$ capacitor. **c**, Maximum charge Q_{max} , residual charge Q_{res} , and reversibly stored charge ΔQ as functions of maximum voltage across the DE-AFE capacitor V_a measured from the waveforms shown in **b**. **d**, Polarization P as a function of extracted electric field E_a across the ZrO_2 layer in a $\text{HfO}_2(8 \text{ nm})/\text{Al}_2\text{O}_3(\sim 1 \text{ nm})/\text{ZrO}_2(10 \text{ nm})$ heterostructure capacitor. The P - E_a characteristics of an equivalent stand-alone ZrO_2 capacitor measured on a conventional ferroelectric tester is also shown for comparison in the background. The negative capacitance regions ($C_{AFE} < 0$) in the P - E_a curve correspond to the capacitance enhancement regions in the ΔQ - V_a curve shown in **c**. **e**, Extracted energy landscape of ZrO_2 . Second derivative of the free energy G with respect to the P based on a polynomial fit is shown below.

From the inversion symmetry of the measured ΔQ - V_a curves in Fig. 3c despite the asymmetric Q_{res} - V_a behavior one can conclude that the capacitive behavior is unaffected by leakage currents or charge injection. Furthermore, a symmetric ΔQ - V_a curve is expected only for an ideal antiferroelectric/dielectric stack with negligible trapped charges at the interface between both layers. This contrasts with recent reports of similar ferroelectric/dielectric capacitors, where large negative trapped charge densities (comparable to the spontaneous polarization) were found at the interface [20] [21]. This indicates that the initial ferroelectric polarization during fabrication in such stacks causes the trapping of charges at the interface, which is not the case for the antiferroelectric heterostructure

due to the non-polar antiferroelectric ground state. Therefore, having a non-polar ground state seems beneficial for avoiding trapped interface charges, which can be detrimental when building negative capacitance devices.

For a given V_a , the electric field in the antiferroelectric layer E_a can be calculated as $E_a = (V_a - V_{DE})/t_{AFE}$, where t_{AFE} is the ZrO_2 thickness and $V_{DE} = \Delta Q(V_a)/C_{DE}$ (see methods for details). The corresponding $P-E_a$ curve ($P = \Delta Q/A$ with A being the area of the capacitor) of the ZrO_2 layer in Fig. 3d shows two separate regions of negative slope (i.e. negative capacitance) which correspond to the capacitance enhancement regions in the $\Delta Q-V_a$ curve in Fig. 3c. For comparison, the $P-E_a$ characteristics of an equivalent, single-layer ZrO_2 capacitor measured using a ferroelectric tester is also plotted in Fig. 3d. The locations of the negative capacitance regions in Fig. 3d coincide with the two hysteresis regions of the polarization-electric field characteristics of the stand-alone ZrO_2 layer, in agreement with the theoretical prediction (Fig. 1a). By integrating the $P-E_a$ curve, one obtains the antiferroelectric energy landscape ($G(P) = \int E_a dP$) which is shown in Fig. 3e, where the normally ‘forbidden’ regions ($G'' < 0$) of thermodynamic instability at the non-polar to polar structural phase transition can be accessed in the antiferroelectric/dielectric heterostructure. It is interesting to note here, that previous first principles calculations for the antiferroelectric transition in ZrO_2 found that G'' is always positive along the direct switching pathway between the $P42/nmc$ and $Pca2_1$ phase, corresponding to a cusp in the energy landscape [24]. This is in contrast to our experimental findings, where negative G'' regions are clearly observed (see Fig. 3e). However, recent first principles calculations have shown that there could be other switching pathways between the $P42/nmc$ and $Pca2_1$ phase, which can avoid the cusp in the energy landscape by traversing through an intermediate orthorhombic $Pmn2_1$ phase [29]. Therefore, our findings provide the first indirect experimental evidence that such an alternative switching pathway might exist in antiferroelectric ZrO_2 .

Next, we changed the HfO_2 thickness to 6 nm and 10 nm while keeping Al_2O_3 and ZrO_2 layer thicknesses constant (~ 1 nm and 10 nm, respectively). For all different HfO_2 thicknesses, the extracted $P-E_a$ characteristics of the ZrO_2 layer have the same quantitative shape as shown in Supplementary Fig. S5-S7. We further observed in Figs. 4a and 4b that the average capacitance enhancement ($r = C_{DE+AFE}/C_{DE} > 1$) in these samples obeys the ideal capacitance matching equation $r = |C_{AFE}|/(|C_{AFE}| - C_{DE})$ with a best fit antiferroelectric negative capacitance $C_{AFE}^o = -4.1 \mu F/cm^2$. Fig. 4c compares the extracted antiferroelectric capacitance as a function of C_{DE} with previous results for multi-domain ferroelectric/dielectric superlattices [31]. Since antiferroelectric ZrO_2 shows ideal capacitance matching behavior, the extracted negative capacitance is constant with C_{DE} . This is in contrast to multi-domain ferroelectric negative capacitance, which strongly depends on the domain configuration and lateral domain wall motion in the ferroelectric and thus on the dielectric and ferroelectric film thickness [32] [33] [34] [35]. On the other hand, the constant $C_{AFE} < 0$ of our antiferroelectric ZrO_2 films with both HfO_2 and ZrO_2 thickness (see also Supplementary Fig. S8) indicates that it is an intrinsic property of the non-polar to polar structural transition. This suggests that antiferroelectricity in ZrO_2 is indeed caused by a local field-induced inversion symmetry breaking of the unit cell. Our findings do not support the recently proposed antiferroelectric model of domain depinning in a depolarized ferroelectric assuming a tetragonal/orthorhombic phase mixture as the ground state [36] [37].

Finally, we simulated an antiferroelectric negative capacitance field-effect transistor (NCFET) based on our experimental results to investigate what performance improvements might be expected compared to current device technologies. The details can be found in the Supplementary Information Section S2. We find that the antiferroelectric NCFET outperforms the reference device in terms of speed while at the same time consuming 41% less power at almost half the power supply voltage (see Supplementary Fig. S9 and Table S1). These results support previous suggestions that antiferroelectrics are indeed promising for ultra-low power electronic devices [38]. Especially since ZrO_2 is already used as the

capacitor dielectric in current dynamic random access memory technologies, which has been demonstrated to also be antiferroelectric [39].

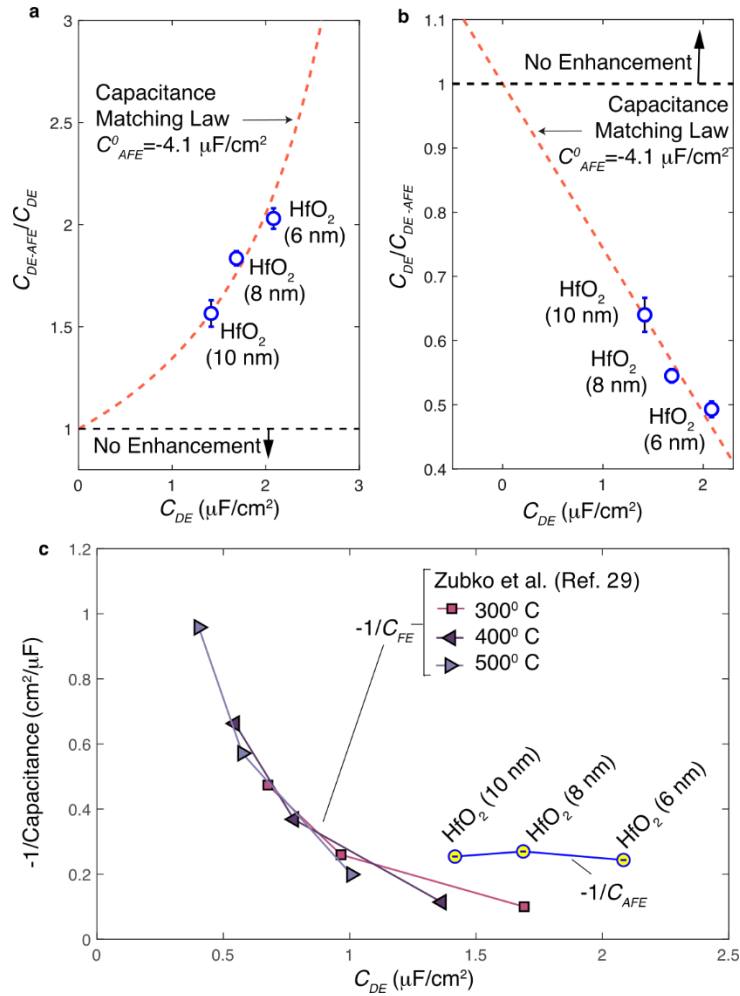


Figure 4. Capacitance matching in antiferroelectric-dielectric heterostructure capacitors. *a,b*, The capacitance enhancement factor $r = C_{DE-AFE}/C_{DE}$ (**a**) and r^{-1} (**b**) in dielectric-antiferroelectric heterostructures with varying HfO₂ thickness as functions of the constituent dielectric capacitance C_{DE} . C_{DE-AFE} is the heterostructure capacitance. The best fit to the capacitance matching law: $C_{DE-AFE}/C_{DE} = |C_{AFE}^0| / (|C_{AFE}^0| - C_{DE})$ is obtained for $C_{AFE}^0 = -4.1 \mu\text{F}/\text{cm}^2$ with a coefficient of determination of $1-3 \times 10^{-2}$, which is also plotted in **a** and **b**. **c**, $-1/\text{Capacitance}$ of the ZrO₂ layer in the heterostructures and of the ferroelectric Pb_{0.5}Sr_{0.5}TiO₃ in ferroelectric-dielectric (paraelectric) SrTiO₃ superlattices reported by Zubko et al. [29]. In each of the Pb_{0.5}Sr_{0.5}TiO₃-SrTiO₃ superlattices, C_{FE} and C_{DE} were calculated assuming that the ferroelectric/dielectric bilayer was repeated 100 times. At each temperature, the effective capacitance of the ferroelectric Pb_{0.5}Sr_{0.5}TiO₃, C_{FE} , was calculated using the relation: $C_{FE+DE} = (C_{DE}^{-1} + C_{FE}^{-1})^{-1}$. The SrTiO₃ capacitance, C_{DE} , was calculated from the temperature evolution of the SrTiO₃ dielectric constant measured in the same work [29]. Note that the negative capacitance of ZrO₂ in this work is independent of C_{DE} whereas the Pb_{0.5}Sr_{0.5}TiO₃ capacitance is a strong function of C_{DE} .

In summary, we have explored the ‘forbidden’ thermodynamic region of the non-polar to polar antiferroelectric transition in ZrO₂ using pulsed electrical measurements for the first time. In contrast to previous reports in multi-domain ferroelectrics, we report a new type of antiferroelectric negative capacitance which seems to be an intrinsic property of the structural instability at the boundary between P4₂/nmc and Pca2₁ phases in fluorite-type oxides. This is of great interest for applications in energy-efficient electronics since mixtures of these phases have been reported in the widely used HfO₂ and ZrO₂ based ultrathin films, which are present in most semiconductor products today. The observation of negative capacitance in ZrO₂ indicates that the switching pathway between the P4₂/nmc and Pca2₁ might include an intermediate ‘saddle’ phase of different symmetry. Furthermore, our findings suggest that the phenomenon of negative capacitance is not limited to polar ferroelectric order but can be expected at any transition with a polarization instability. This includes phase

transitions between non-polar and polar phases as shown here, but which should also include transitions between different polar phases or even between different non-polar phases [40]. This opens up new opportunities for characterizing structural phase transitions and for building negative capacitance devices from a much broader range of possible materials.

References

- [1] S. Patel, A. Chauhan und R. Vaish, „A technique for giant mechanical energy harvesting using ferroelectric/antiferroelectric materials,“ *Journal of Applied Physics*, Bd. 115, p. 084908, 2014.
- [2] M. H. Park, H. J. Kim, Y. J. Kim, T. Moon, K. D. Kim und C. S. Hwang, „Toward a multifunctional monolithic device based on pyroelectricity and the electrocaloric effect of thin antiferroelectric HfxZr1-xO2 films,“ *Nano Energy*, Bd. 12, pp. 131-140, 2015.
- [3] B. Xua, L. E. Cross und J. J. Bernstein, „Ferroelectric and antiferroelectric films for microelectromechanical systems applications,“ *Thin Solid Films*, Bde. %1 von %2377-378, pp. 712-718, 2000.
- [4] H. Wang, Y. Liu, T. Yang und S. Zhang, „Ultrahigh Energy-Storage Density in Antiferroelectric Ceramics with Field-Induced Multiphase Transitions,“ *Advanced Functional Materials*, Bd. 29, p. 1807321, 2019.
- [5] B. Xu, J. Íñiguez und L. Bellaiche, „Designing lead-free antiferroelectrics for energy storage,“ *Nature Communications*, Bd. 8, p. 15682, 2017.
- [6] C. Kittel, „Theory of Antiferroelectric Crystals,“ *Physical Review*, Bd. 82, pp. 729-732, 1951.
- [7] E. Sawaguchi, H. Maniwa und S. Hoshino, „Antiferroelectric Structure of Lead Zirconate,“ *Physical Review*, Bd. 83, p. 1078, 1951.
- [8] G. Shirane, E. Sawaguchi und Y. Takagi, „Dielectric Properties of Lead Zirconate,“ *Physical Review*, Bd. 84, pp. 476-481, 1951.
- [9] Z. Wu, X. Liu, C. Ji, L. Li, S. Wang, Y. Peng, K. Tao, Z. Sun, M. Hong und J. Luo, „Discovery of an Above-Room-Temperature Antiferroelectric in Two-Dimensional Hybrid Perovskite,“ *Journal of the American Chemical Society*, Bd. 141, pp. 3812-3816, 2019.
- [10] R. Ramesh und D. G. Schlom, „Creating emergent phenomena in oxide superlattices,“ *Nature Reviews Materials*, Bd. 4, pp. 157-268, 2019.
- [11] T. S. Böscke, J. Müller, D. Bräuhäus, U. Schröder und U. Böttger, „Ferroelectricity in hafnium oxide thin films,“ *Applied Physics Letters*, Bd. 99, p. 102903, 2011.
- [12] J. Müller, T. S. Böscke, U. Schröder, S. Mueller, D. Bräuhäus, U. Böttger, L. Frey und T. Mikolajick, „Ferroelectricity in Simple Binary ZrO2 and HfO2,“ *Nano Letters*, Bd. 12, p. 4318-4323, 2012.
- [13] J. W. Bennett, K. F. Garrity, K. M. Rabe und D. Vanderbilt, „Orthorhombic ABC Semiconductors as Antiferroelectrics,“ *Physical Review Letters*, Bd. 110, p. 017603, 2013.
- [14] H. Aramberri und J. Íñiguez, „Antiferroelectricity in a family of pyroxene-like oxides with rich polymorphism,“ *Communications Materials*, Bd. 1, p. 52, 2020.

- [15] K. M. Rabe, „Antiferroelectricity in Oxides: A Reexamination,“ in *Functional Metal Oxides: New Science and Novel Applications*, Wiley-VCH Verlag GmbH & Co. KGaA, 2013, pp. 221-244.
- [16] P. Tolédano und M. Guennou, „Theory of antiferroelectric phase transitions,“ *Physical Review B*, Bd. 94, p. 014107, 2016.
- [17] R. Landauer, „Can capacitance be negative?,“ *Collective Phenomena*, Bd. 2, p. 167–170, 1976.
- [18] S. Salahuddin und S. Datta, „Use of Negative Capacitance to Provide Voltage Amplification for Low Power Nanoscale Devices,“ *Nano Letters*, Bd. 8, pp. 405-410, 2008.
- [19] W. J. Merz, „Double Hysteresis Loop of BaTiO₃ at the Curie Point,“ *Physical Review*, Bd. 91, pp. 513-517, 1953.
- [20] Y. J. Kim, H. Yamada, T. Moon, Y. J. Kwon, C. H. An, H. J. Kim, K. D. Kim, Y. H. Lee, S. D. Hyun, M. H. Park und C. S. Hwang, „Time-Dependent Negative Capacitance Effects in Al₂O₃/BaTiO₃ Bilayers,“ *Nano Letters*, Bd. 16, p. 4375–4381, 2016.
- [21] M. Hoffmann, F. P. G. Fengler, M. Herzig, T. Mittmann, B. Max, U. Schroeder, R. Negrea, P. Lucian, S. Slesazek und T. Mikolajick, „Unveiling the double-well energy landscape in a ferroelectric layer,“ *Nature*, Bd. 565, p. 464–467, 2019.
- [22] M. Hoffmann, F. P. G. Fengler, B. Max, U. Schroeder, S. Slesazek und T. Mikolajick, „Negative Capacitance for Electrostatic Supercapacitors,“ *Advanced Energy Materials*, Bd. 9, p. 1901154, 2019.
- [23] A. K. Tagantsev, K. Vaideswaran, S. B. Vakhrushev, A. V. Filimonov, R. G. Burkovsky, A. Shaganov, D. Andronikova, A. I. Rudskoy, A. Q. R. Baron, H. Uchiyama, D. Chernyshov, A. Bosak, Z. Ujma, K. Roleder, A. Majchrowski, J.-H. Ko und N. Setter, „The origin of antiferroelectricity in PbZrO₃,“ *Nature Communications*, Bd. 4, p. 2229, 2013.
- [24] S. E. Reyes-Lillo, K. F. Garrity und K. M. Rabe, „Antiferroelectricity in thin-film ZrO₂ from first principles,“ *Physical Review B*, Bd. 90, p. 140103(R), 2014.
- [25] M. H. Park und C. S. Hwang, „Fluorite-structure antiferroelectrics,“ *Reports on Progress in Physics*, Bd. 82, p. 124502, 2019.
- [26] X. Sang, E. D. Grimley, T. Schenk, U. Schroeder und J. M. LeBeau, „On the structural origins of ferroelectricity in HfO₂ thin films,“ *Applied Physics Letters*, Bd. 106, p. 162905, 2015.
- [27] S. Lombardo, C. Nelson, K. Chae, S. Reyes-Lillo, M. Tian, N. Tasneem, Z. Wang, M. Hoffmann, D. Triyoso, S. Consiglio, K. Tapily, R. Clark, G. Leusink, K. Cho, A. Kummel, J. Kacher und A. Khan, „Atomic-scale imaging of polarization switching in an (anti-) ferroelectric memory material: Zirconia (ZrO₂),“ in *2020 IEEE Symposium on VLSI Technology*, Honolulu, HI, USA, 2020.
- [28] R. Materlik, C. Künneth und A. Kersch, „The origin of ferroelectricity in Hf_{1-x}Zr_xO₂: A computational investigation and a surface energy model,“ *Journal of Applied Physics*, Bd. 117, p. 134109, 2015.
- [29] Y. Qi und K. M. Rabe, „Phase competition in HfO₂ with applied electric field from first principles,“ *Physical Review B*, Bd. 102, p. 214108, 2020.

- [30] M. Hoffmann, B. Max, T. Mittmann, U. Schroeder, S. Slesazeck und T. Mikolajick, „Demonstration of High-speed Hysteresis-free Negative Capacitance in Ferroelectric Hf_{0.5}Zr_{0.5}O₂,“ in *International Electron Devices Meeting (IEDM) 2018*, San Francisco, CA, USA, 2018.
- [31] P. Zubko, J. C. Wojdeł, M. Hadjimichael, S. Fernandez-Pena, A. Sené, I. Luk'yanchuk, J.-M. Triscone und J. Íñiguez, „Negative capacitance in multidomain ferroelectric superlattices,“ *Nature*, Bd. 534, p. 524–528, 2016.
- [32] H. W. Park, J. Roh, Y. B. Lee und C. S. Hwang, „Modeling of Negative Capacitance in Ferroelectric Thin Films,“ *Advanced Materials*, Bd. 31, p. 1805266, 2019.
- [33] J. Íñiguez, P. Zubko, I. Luk'yanchuk und A. Cano, „Ferroelectric negative capacitance,“ *Nature Reviews Materials*, Bd. 4, p. 243–256, 2019.
- [34] A. K. Yadav, K. X. Nguyen, Z. Hong, P. García-Fernández, P. Aguado-Puente, C. T. Nelson, S. Das, B. Prasad, D. Kwon, S. Cheema, A. I. Khan, C. Hu, J. Íñiguez, J. Junquera, L.-Q. Chen, D. A. Muller, R. Ramesh und S. Salahuddin, „Spatially resolved steady-state negative capacitance,“ *Nature*, Bd. 565, p. 468–471, 2019.
- [35] S. Das, Z. Hong, V. A. Stoica, M. A. P. Gonçalves, Y. T. Shao, E. Parsonnet, E. J. Marks, S. Saremi, M. R. McCarter, A. Reynoso, C. J. Long, A. M. Hagerstrom, D. Meyers, V. Ravi, B. Prasad, H. Zhou und Z. Zhang, „Local negative permittivity and topological phase transition in polar skyrmions,“ *Nature Materials*, Bd. 20, p. 194–201, 2021.
- [36] P. D. Lomenzo, C. Richter, T. Mikolajick und U. Schroeder, „Depolarization as Driving Force in Antiferroelectric Hafnia and Ferroelectric Wake-Up,“ *ACS Applied Electronic Materials*, Bd. 2, p. 1583–1595, 2020.
- [37] P. D. Lomenzo, M. Materano, C. Richter, R. Alcala, T. Mikolajick und U. Schroeder, „A Gibbs energy view of double hysteresis in ZrO₂ and Si-doped HfO₂,“ *Applied Physics Letters*, Bd. 117, p. 142904, 2020.
- [38] K. Karda, A. Jain, C. Mouli und M. A. Alam, „An anti-ferroelectric gated Landau transistor to achieve sub-60 mV/dec switching at low voltage and high speed,“ *Applied Physics Letters*, Bd. 106, p. 163501, 2015.
- [39] M. Pešić, M. Hoffmann, C. Richter, T. Mikolajick und U. Schroeder, „Nonvolatile Random Access Memory and Energy Storage Based on Antiferroelectric Like Hysteresis in ZrO₂,“ *Advanced Functional Materials*, Bd. 26, pp. 7486-7494, 2016.
- [40] A. Lai und C. Schuh, „Direct Electric-Field Induced Phase Transformation in Paraelectric Zirconia via Electrical Susceptibility Mismatch,“ *Physical Review Letters*, Bd. 126, p. 015701, 2021.
- [41] V. Mukundan, K. Beckmann, K. Tapily, S. Consiglio, R. Clark, G. Leusink, N. Cady und A. C. Diebold, „Structural Correlation of Ferroelectric Behavior in Mixed Hafnia-Zirconia High-k Dielectrics for FeRAM and NCFET Applications,“ *MRS Advances*, Bd. 4, p. 545–551, 2019.

Methods

Sample fabrication. The atomic layer deposition (ALD) of ZrO_2 and bottom TiN layers were conducted in a 300 mm Tokyo Electron thin film formation tool. The ZrO_2 and TiN films were deposited by ALD using previously described processes [41]. The as-grown ZrO_2 layer was amorphous. With regards to the thickness of ZrO_2 in the ZrO_2/TiN heterostructure of these samples, there were two differently processed stacks: ZrO_2/TiN with 10 nm ZrO_2 and 5 nm ZrO_2 , respectively. A post- ZrO_2 deposition annealing was performed on both stacks at 450 °C for 30 seconds in nitrogen atmosphere to stabilize the ZrO_2 layer in the antiferroelectric tetragonal phase. The ZrO_2/TiN heterostructure was cleaned in standard clean-2 (SC-2) solution. Afterwards, HfO_2 (6, 8, 10 nm)/ Al_2O_3 (~1 nm) heterostructure was deposited on the ZrO_2/TiN heterostructure in a Cambridge NanoTech Fiji G2 Plasma Enhanced ALD (PEALD) system at Georgia Tech. Subsequently, a top TiN layer was deposited without breaking the vacuum in the same ALD reactor. The deposition was carried out at 250 °C using tetrakis (dimethylamido) hafnium, tetrakis (dimethylamido) aluminum and tetrakis (dimethylamido) titanium precursors for HfO_2 , Al_2O_3 and TiN, respectively. For oxides, water was used as the oxygen source and for TiN, nitrogen (plasma) was used as the nitride source. After the ALD of TiN/ $\text{HfO}_2/\text{Al}_2\text{O}_3/\text{ZrO}_2/\text{TiN}$ and TiN/ $\text{HfO}_2/\text{ZrO}_2/\text{TiN}$ heterostructures, Al (~100 nm) was evaporated and patterned into rectangular electrodes using standard microfabrication techniques. Top TiN layer was wet etched afterwards in $\text{H}_2\text{O}_2:\text{H}_2\text{O}$ solution at 50 °C using the patterned Al layer as a hard mask.

Electrical characterization. Electrical measurements were conducted on a Cascade Microtech Summit 1200K Semi-automated Probe Station. Polarization versus electric field curves were measured using an aixACCT TF-3000 ferroelectric parameter analyzer at 1 kHz with dynamic leakage current compensation (DLCC) turned off. The capacitance versus electric field curves were measured by a Keysight E4990A impedance analyzer with a small-signal amplitude of 25 mV and a frequency of 100 kHz. The pulsed measurements on dielectric/antiferroelectric heterostructure capacitors were conducted using a Keysight 81150A Pulse Function Arbitrary Noise Generator and a Keysight DSOS104A Oscilloscope. The series resistor had a resistance of $R = 5.6 \text{ k}\Omega$.

Structural characterization. X-ray diffraction (XRD) measurements were performed using SmartLab diffractometer (Rigaku) equipped with 9 kW copper rotating anode X-ray source (wavelength $\text{CuK}\alpha = 0.15418 \text{ nm}$). A standard co-planar diffraction geometry with constant angle of incidence (grazing incidence X-ray diffraction: GIXRD) was used for the studies. To perform the GIXRD measurements the diffractometer was equipped with a parabolic multilayered X-ray mirror and a set of axial divergence eliminating soller slits with divergence of 5° in incident and diffracted beam, and parallel plate collimator with acceptance of 0.5° in diffracted beam. Diffracted intensity was acquired with hybrid-pixel single photon counting 2D detector HyPix 3000. The incidence angle of the X-rays, with respect to the sample surface, was set up slightly above the critical angle of investigated material, $\omega = 0.6^\circ$. Measured diffraction data were fitted using whole powder pattern procedure - Rietveld method. A computer program MStruct was used for the fitting. The investigated samples contain tetragonal ZrO_2 phase (space group $\text{P}4_2/\text{nmc}$, #137). Some minor fractions of other ZrO_2 phases might be present, but in fractions below the detection limit of GIXRD. Scanning transmission electron microscopy (STEM) imaging was performed using a Hitachi aberration corrected STEM HD2700 operating at 200 kV at Georgia Tech. The convergent angle is 35 mrad, and the inner angle of the annular dark field (ADF) detector is 50 mrad. Nano beam electron diffraction (NBED) was performed using a FEI transmission electron microscope (TEM) Technai F30 working at 300 kV. The determination of the phase of ZrO_2 was accomplished by analyzing the NBED patterns.

Extraction of antiferroelectric P-E_a characteristics from pulsed measurements. Voltage pulses V_{in} of duration $T = 1.1 \mu\text{s}$ with different amplitudes were applied, and the voltage across the dielectric/antiferroelectric capacitor, $V_{\text{DE-AFE}}$ and V_{in} were measured using an oscilloscope. The input

pulse amplitude V_{in} was changed in 200 mV steps to span the full P- E_a curves. At a given applied voltage amplitude V_a , voltages across the dielectric layers and the antiferroelectric layer was calculated as $V_{DE} = \Delta Q/C_{DE}$ and $V_{AFE} = V_a - V_{DE}$, respectively. For each of the dielectric/antiferroelectric samples, an equivalent dielectric only stack with the same thicknesses of HfO_2 and Al_2O_3 (~1 nm) layers was deposited under the same process conditions to measure C_{DE} independently (measurements shown in Fig. S4). Fig. 3d as well as Fig. S5, S6c, S7c and Fig. S8a show the polarization $P = \Delta Q/A$ as a function of the extracted electric field in the antiferroelectric $E_a = V_{AFE}/t_a$ where A and t_a are the capacitor area and the ZrO_2 thickness. The details of the calculations are provided below.

The voltage V_{in} applied to the system can be written as

$$V_{in} = IR + V_{DE-AFE} \quad (1)$$

with

$$V_{DE-AFE} = V_D + V_{AFE}, \quad (2)$$

where V_{DE-AFE} , V_{DE} , and V_{AFE} are the voltages across the entire dielectric/antiferroelectric heterostructure, dielectric combo, and antiferroelectric layer, respectively. The current $I(t)$ flowing through the resistor R in series with the dielectric/antiferroelectric heterostructure is calculated from measured $V_{in}(t)$ and $V_{DE-AFE}(t)$ waveforms. The amount of charge Q on the heterostructure capacitor is calculated by

$$Q(t) = \int I(t)dt - C_{para}V_{DE-AFE}(t), \quad (3)$$

where C_{para} is the parasitic capacitance that appears in parallel to the dielectric/antiferroelectric capacitor, which was experimentally determined as ~20 pF. Three important charges are extracted for each value of V_a : the maximum stored charge on the capacitor, $Q_{max} = Q(t=T)$, the residual charge on the capacitor after the applied voltage is zero again, $Q_{res} = Q(t=5 \mu s \gg T)$, and the charge that is reversibly stored and released from the capacitor, $\Delta Q = Q_{max} - Q_{res}$. The electric field E_a in the antiferroelectric layer can be calculated by

$$E_a = \frac{1}{t_a} \left(V_a - \frac{\Delta Q}{C_{DE}} \right), \quad (4)$$

where ΔQ is the amount of charges reversed and C_{DE} is the capacitance of the dielectric layer. The relative permittivity ϵ_r of the dielectric layers was extracted from capacitance versus voltage measurements on samples fabricated without the antiferroelectric layer (see supplementary Fig. S4). The polarization of the antiferroelectric layer was calculated as

$$P = \frac{\Delta Q}{A} - \epsilon_0 E_a \approx \frac{\Delta Q}{A}, \quad (5)$$

where A is the area of the dielectric/antiferroelectric capacitor. Using Eq. (4) and (5), the antiferroelectric P versus E_a curve can be calculated. The experimental free energy density G can be obtained from

$$G = \int E_a(P)dP. \quad (6)$$

Data availability

The data generated and analyzed in this study are available from the corresponding authors upon reasonable request.

Acknowledgements

This work was supported in part by the National Science Foundation, in part by the Global Research Collaboration (GRC) program of the Semiconductor Research Corporation (SRC) and in part by the Applications and Systems-Driven Center for Energy-Efficient Integrated Nano Technologies (ASCENT), one of six centers in the Joint University Microelectronics Program (JUMP), an SRC program sponsored by the Defense Advanced Research Program Agency (DARPA). This work was performed in part at the Georgia Tech Institute for Electronics and Nanotechnology, a member of the National Nanotechnology Coordinated Infrastructure (NNCI), which is supported by the National Science Foundation (ECCS-1542174). M.D. acknowledges the financial support from the project NanoCent-Nanomaterials Centre for Advanced Applications, Project No. CZ.02.1.01/0.0/0.0/15_003/0000485 financed by ERDF. S.E.R.-L. acknowledged support from the supercomputing infrastructure of the NLHPC (ECM-02) and Fondo Nacional de Desarrollo Científico y Tecnológico (FONDECYT, Chile) through the program Iniciación en Investigación 2018 under Grant No. 11180590. Y.L. and J.R. acknowledge the support from Air Force Office of Scientific Research under award no. FA9550-16-1-0335. This work was financially supported out of the State budget approved by the delegates of the Saxon State Parliament.

Author Contributions

Z.W., N.T., M.H. and A.I.K conceived the experiment. Z.W. and N.T. performed the electrical measurements. N.T. led the growth using the ALD technique and the capacitor fabrication steps at Georgia Tech. S.C. and K.T. performed ALD of ZrO₂/TiN heterostructure using a 300 mm Tokyo Electron thin film formation tool. M.T. performed the TEM experiments. S.S.K.P. performed the modeling of AFE NCFETs. Z.W., N.T., M.H., M.T., J.K., S.E.R.-L., J.R., A.I.K. wrote the initial manuscript. All authors discussed the results and gave inputs to the final manuscript.

Competing Interests

The authors declare that they have no competing financial interests.